A New Minimum-Volume Enclosing Algorithm for Endmember Identification and Abundance Estimation in Hyperspectral Data

Eligius M. T. Hendrix, Inmaculada García, Javier Plaza, Gabriel Martín, and Antonio Plaza, *Senior Member, IEEE*

***Abstract*—Spectral unmixing is an important technique for hyperspectral data exploitation, in which a mixed spectral signature is decomposed into a collection of spectrally pure constituent spectra, called *endmembers*, and a set of correspondent fractions, or *abundances*, that indicate the proportion of each endmember present in the mixture. Over the last years, several algorithms have been developed for automatic or semiautomatic endmember extraction. Some available approaches assume that the input data set contains at least one pure spectral signature for each distinct material and further conduct a search for the most spectrally pure signatures in the high-dimensional space spanned by the hyperspectral data. Among these approaches, those aimed at maximizing the volume of the simplex that can be formed using available spectral signatures have found wide acceptance. However, the presence of spectrally pure constituents is unlikely in remotely sensed hyperspectral scenes due to spatial resolution, mixing phenomena, and other considerations. In order to address this issue, other available algorithms have been developed to generate *virtual* endmembers (not necessarily present among the input data samples) by finding the simplex with minimum volume that encloses all available observations. In this paper, we discuss maximum-volume versus minimum-volume enclosing solutions and further develop a novel algorithm in the latter category which incorporates the fractional abundance estimation as an internal step of the endmember searching process (i.e., it does not require an external method to produce endmember fractional abundances). The method is based on iteratively enclosing the observations in a lower dimensional space and removing observations that are most likely not to be enclosed by the simplex of the endmembers to be estimated. The performance of the algorithm is investigated and compared to that of other algorithms (with and without the pure pixel assumption) using synthetic and real hyperspectral data sets collected by a variety of hyperspectral imaging instruments.**

***Index Terms*—Endmember extraction, fractional abundance estimation, hyperspectral imaging, maximum-volume simplex, minimum-volume enclosing simplex (MVES), spectral unmixing.**

Manuscript received July 20, 2010; revised March 18, 2011 and August 10, 2011; accepted October 23, 2011. Date of publication December 19, 2011; date of current version June 20, 2012. This work was supported in part by the European Community's Marie Curie Research Training Networks Program under Reference MRTN-CT-2006-035927, Hyperspectral Imaging Network, by the Spanish Ministry of Science and Innovation under Grants AYA2008-05965-C04-02 and TIN2008-01117, by the Junta de Andalucia under Projects P06-TIC-01426 and P08-TIC-3518, by the European Regional Development Fund, and by the Junta de Extremadura (local government) under Project PRI09A110.

E. M. T. Hendrix and I. García are with the Department of Computer Architecture, University of Málaga, 29071 Málaga, Spain (e-mail: Eligius.Hendrix@wur.nl; igarcia@ual.es).

J. Plaza, G. Martín, and A. Plaza are with the Hyperspectral Computing Laboratory, University of Extremadura, 10003 Cáceres, Spain (e-mail: jplaza@unex.es; gamahefpi@unex.es; aplaza@unex.es).

Color versions of one or more of the figures in this paper are available online at http://ieeexplore.ieee.org.

Digital Object Identifier 10.1109/TGRS.2011.2174443

I. Introduction

SPECTRAL unmixing is an important tool for remotely sensed hyperspectral data interpretation [1]. Due to the available spatial resolution, most of the pixels (vectors) collected by the latest generation imaging spectrometers such as the National Aeronautics and Space Administration Jet Propulsion Laboratory's Airborne Visible/Infrared Imaging Spectrometer (AVIRIS) [2]—with a spatial resolution of 20 m per pixel and 224 spectral bands comprised between 0.4 and 2.5 μm—are mixed in nature [3]. Consider a hyperspectral scene with $i = 1, \ldots, m$ spectral bands and $k = 1, \ldots, r$ m-dimensional pixel vectors x modeled by

$$x = Ea + \epsilon \tag{1}$$

where $E = [e_1, e_2, \ldots, e_n]$ is an $m \times n$ matrix containing a set of n pure spectral constituents (*endmembers*) and a is an n-dimensional vector containing the fractional abundance of each of the n endmembers in the pixel x. Finally, ϵ is an m-dimensional vector of white Gaussian noise with standard deviation σ. The final goal of an endmember extraction method is to recover the matrix E and the endmember fractional abundance a for each observed pixel. To do so, usually, noise needs to be minimized (in least squares fashion), and the volume of the simplex spanned by the columns of matrix E should be minimized [4]. Moreover, the abundances should be positive for each entry in the $m \times r$ matrix of band observations (nonnegativity constraint), and the sum of all endmember abundances in a given pixel should add up to unity (sum-to-one constraint) [5]. The question is how to deal with least squares and minimum volume in such a way that the estimation is unbiased, i.e., the expected value of the estimator is the real value. When applying the idea of least squares during the estimation procedure, we encounter a first problem in the fact that, often, the number of endmembers is not known in advance, and an external technique is required for estimating this number [6], [7]. Also, techniques based on principal component analysis (PCA) [8] or maximum noise fraction [9] can be used for dimension reduction. In other words, if we assume that n endmembers are sufficient to characterize mixed pixels in the scene, the goal is to discover an $(n-1)$-dimensional subspace responsible for the main variations, while the rest of the m-dimensional space can be considered noise. It should be noted that several techniques have been developed to automatically estimate the number of endmembers n in practice. Examples include the virtual

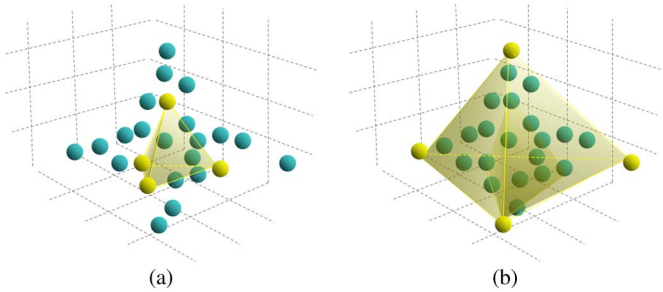

Fig. 1. Graphical interpretation of the N-FINDR maximum-volume estimation algorithm in a 3-D space. (a) N-FINDR initialized randomly. (b) Final volume estimation by N-FINDR.

dimensionality concept [6] or the hyperspectral subspace identification by minimum error [7].

Over the last years, several algorithms have also been developed for automatic or semiautomatic estimation of endmembers in matrix E by assuming that the input hyperspectral data set contains at least one pure observation for each distinct material present in the collected scene, and therefore, a search procedure aimed at finding the most spectrally pure signatures in the input scene is feasible [10]. Techniques include, among many others [11], [12], the orthogonal subspace projection (OSP) algorithm [13], the N-FINDR algorithm [4], the vertex component analysis (VCA) algorithm [14], and spatial–spectral approaches such as the automatic morphological endmember extraction (AMEE) [15], a spatial preprocessing (SPP) technique [16], and a region-based SPP (RBSPP) technique [17]. Several other techniques for endmember extraction and spectral unmixing have been recently developed under the pure pixel assumption [18]–[27]. Volume-inflating techniques, of which N-FINDR is a representative algorithm, have found wide acceptance in the community [28]. This technique looks for the set of pixels with the largest possible volume by inflating a simplex inside the data [29]. The procedure begins with a random initial selection of pixel vectors [see Fig. 1(a)]. Every pixel must be evaluated in order to refine the initial estimate of endmembers, looking for the set of pixels that maximize the volume of the simplex defined by selected endmembers. The corresponding volume is calculated for every pixel in each endmember position by replacing that endmember and finding the resulting volume. If the replacement results in an increase of volume, the pixel replaces the candidate endmember. This procedure is repeated until no improvement is found [see Fig. 1(b)].

Although the procedure adopted by N-FINDR is successful if pure pixels are present in the data, given the spatial resolution of state-of-the-art imaging spectrometers and the presence of the mixture phenomenon at different scales (even at microscopic levels), this assumption may no longer be valid, and most of the pixels may be mixed in nature. Other methods have been developed for endmember extraction that do not assume the presence of pure signatures in the input data. Instead, these methods aim at generating *virtual* endmembers [30] (not necessarily present in the set composed of input data samples and most likely without physically meaningful spectral signatures) by finding the simplex with minimum volume that encompasses all observations. Techniques in this category include convex cone analysis [31], iterative constrained endmembers (ICEs) [32], a sparsity-promoting version of this algorithm (SPICE) [33], dependent component analysis [34], or optical real-time adaptive spectral identification system [35]. The normal compositional model initially introduced in [36] has been shown in [37] to have good unmixing properties when there are few or no pure pixels in the image. Also included in this category are volume minimization approaches inspired by the seminal minimum-volume transform (MVT) algorithm [38], such as the minimum-volume simplex analysis (MVSA) algorithm [39], the convex-analysis-based minimum-volume enclosing simplex (MVES) algorithm [40], or the minimum-volume constrained nonnegative matrix factorization (MVC-NMF) method [41]. Other methods based on the NMF have been recently developed for spectral unmixing purposes [42], [43].

Having n endmembers and the observed data set containing sufficient (e.g., $n-1$) points on each facet, the principle of minimum-volume-based methods is that the vertices can be inferred by seeking for the simplex with minimum volume to which all the observed pixel vectors belong, without the need for using real pixels as vertices. MVT-inspired algorithms can first reduce the dimensionality of the input data from m to $n-1$ and then apply the aforementioned concept (in iterative fashion) until a set of n endmembers has been derived. Once the (possibly virtual) endmembers have been derived, an abundance estimation process usually follows in order to determine the contribution of each endmember to each observed pixel. Several MVT-based methods, however, perform endmember extraction and abundance estimation simultaneously (e.g., MVC-NMF or ICE). It should be noted that noise in hyperspectral imaging instruments is relatively low. As a result, standard least squares approaches such as the fully constrained linear spectral unmixing [5] have been widely used for abundance estimation. However, these methods generally assume that pure spectral signatures are available in the input data, which may not be the case. To address this issue, the MVSA replaces the hard constraints on the abundance fractions with a hinge-type loss function [39] to account for outliers and noise. Other algorithms such as MVC-NMF or SPICE use a weight to balance a least-squares-related term and a volume-related term, which are minimized into a single objective function.

In this paper, we present and investigate a new method for endmember identification (called MINVEST) which follows the MVT principle. First, it uses a dimensionality reduction technique to bring the dimensionality of the data from m to $n-1$, and second, it minimizes the volume of an enclosing simplex in the reduced space while estimating the fractional abundance of vertices simultaneously. The novel feature of MINVEST is that it takes care of noise by iteratively identifying and removing pixels that fall outside the simplex to be estimated. In addition, MINVEST estimates fractional abundances during the endmember identification process. In other words, the method does not require an external abundance estimation module to produce fully constrained endmember fractional abundances. This is a highly desirable feature in techniques aimed at deriving virtual endmembers since the spectral signatures associated to such endmembers often lack physical interpretation [35] and, therefore, might not be feasible

for an abundance estimation process such as the one conducted under the assumption that pure pixels are present in the input data. Recently, a similar approach has been developed using sequential linear programming to solve the MVES problem [40], [44]. As will be shown, standard available nonlinear optimization algorithms can be used to solve the same problem.

The remainder of this paper is organized as follows. Section II describes the method and its underlying principles. Section III provides a detailed experimental assessment of the performance of the method using a database of synthetic hyperspectral scenes generated using fractals and a real hyperspectral data set collected by AVIRIS. In all cases, the performance is compared to that of state-of-the-art techniques for endmember extraction which assume the presence of pure pixels [OSP, N-FINDR, VCA, spatial–spectral endmember extraction (SSEE), AMEE, SPP, and RBSPP] and also to that of techniques that do not incorporate such assumption (MVES and MVSA). Section IV concludes with some remarks and hints at plausible future research.

II. Minimum-Volume Simplicial Enclosure Method

A. Principle of Volume Reduction

Linear spectral unmixing methods [3] exploit the idea that the observations x in m-dimensional space ($m = 224$ spectral bands for the AVIRIS imaging spectrometer) are in reality combinations of only n endmembers. This means that observations in the space $\mathbb{E} = \{x = Ea | a \in \mathbb{R}^n, \sum_i a_i = 1\} \subset \mathbb{R}^m$ can be represented by points in $\mathbb{V} = \{z = Va | a \in \mathbb{R}^n, \sum_i a_i = 1\} \subset \mathbb{R}^{n-1}$, which is much lower in dimension, i.e., $n \ll m$, where $V = [v_1, \ldots, v_n]$ is an $(n-1) \times n$ matrix of the so-called vertices v_i. The transformation is based on some observations from linear algebra and works as follows.

Let E^- be the matrix $E^- = [e_2 - e_1, e_3 - e_1, \ldots, e_n - e_1]$. Its columns span the linear space $\langle E^- \rangle$ such that one can write $\mathbb{E}$ as $\mathbb{E} = \{x = e_1 + E^- y | y \in \mathbb{R}^{n-1}\}$. More precisely, let Γ be a matrix where its columns form an orthonormal basis of $\langle E^- \rangle$. The number of columns of Γ is equal to the rank of $\langle E^- \rangle$. The rank is $n-1$ if the columns of E are affine independent. This means that the space $\mathbb{E}$ can be described as $\mathbb{E} := \{x = b + \Gamma d | d \in R^{n-1}\}$, with b as an arbitrary given m-vector in $\mathbb{E}$ and Γ as an arbitrary $m \times (n-1)$ orthonormal matrix, such that $\langle \Gamma \rangle = \langle E^- \rangle$, i.e., its columns have length 1 and are orthogonal with respect to each other. Now, given a choice for b and $\langle \Gamma \rangle$, let the vertices v_i be solutions of

$$\Gamma v_i = e_i - b, \qquad i = 1, \ldots, n. \tag{2}$$

Then, in matrix notation, we have $E = \Gamma V + b\mathbf{1}^{\mathrm{T}}$, where $\mathbf{1}$ is the all-one vector of appropriate dimension. For each abundance vector a (keep in mind that its elements sum to one), we have a unique point $x \in \mathbb{E}$ as well as $z \in \mathbb{V}$ related as $x = Ea = (\Gamma V + b\mathbf{1}^{\mathrm{T}})a = \Gamma z + b$.

Two questions arise at this point: 1) What choices are convenient for b and Γ? and 2) what are the consequences for model (1), which includes white noise, if we have such a vector b and orthonormal basis matrix Γ? To start with the latter, let us consider the so-called score vector z in $(n-1)$-dimensional space

$$z = Va + \xi \tag{3}$$

where $\Gamma\xi$ is the projection of ϵ on the space $\langle \Gamma \rangle$. It can be derived that ξ is white noise. Due to Γ being orthonormal, $\Gamma^{\mathrm{T}}\Gamma$ is the unit matrix, and the projection leads to $\xi = (\Gamma^{\mathrm{T}}\Gamma)^{-1}\Gamma^{\mathrm{T}}\epsilon = \Gamma^{\mathrm{T}}\epsilon$. Notice that the variance–covariance matrix of ξ is $\Gamma^{\mathrm{T}}\Gamma$, i.e., the unit matrix. The relation of (3) with the original model (1) is

$$\begin{aligned}(x - b) &= Ea - b + \epsilon = \Gamma V a + \epsilon \\ &= \Gamma(Va + \xi) + \zeta = \Gamma z + \zeta\end{aligned} \tag{4}$$

where ζ is the projection of ϵ on the orthoplement of $\langle \Gamma \rangle$. So in fact, ϵ is decomposed into $\epsilon = \Gamma\xi + \zeta$. The consequence of these algebraic observations and the underlying stochastic model is that, given a support vector b and matrix Γ, the original model (1) in m-dimensional space reduces to model (3) in $(n-1)$-dimensional space. The observations $X = [x_1, \ldots, x_r]$ that, without noise, would lay in the simplex constituted by the so-called convex hull of E, $\mathrm{conv}(E) \subset \mathbb{E}$, have a one-to-one relation with their representation $Z = [z_1, \ldots, z_r]$ in simplex $S = \mathrm{conv}(V)$. Given these observations, a desirable objective is to find out the endmember representation V and the original endmember signals in E; this process is called endmember identification.

In [41], a matrix factorization approach is used that simultaneously minimizes least squares and the simplex volume for endmember generation. For volume reduction, it is good to add a direction without variation to the principal components; zero variation gives zero volume. In turn, the least squares idea looks for directions with maximum variation. Miao and Qi [41] use weights to deal with these two objectives. In this paper, we follow a similar strategy based on estimating the number of interior/exterior points by weighting these two terms. Specifically, we investigate a procedure which takes a hierarchical approach by first estimating the subspace $\mathbb{E}$ in which the n endmembers are lying by means of PCA (a similar approach was adopted in [45]).

The choice of using PCA means that space $\mathbb{E} = b + \langle \Gamma \rangle$ is estimated by taking $b = \overline{x} = (1/r)\sum_j x_j$ and $\Gamma = C = [c_1, \ldots, c_{n-1}]$ is an $m \times (n-1)$ matrix of principal components; we have the biggest variation in direction c_1, the second biggest in direction c_2, etc. Following this procedure, the (unknown) scores z_k are estimated from observations x_k by taking $z_k = (C^{\mathrm{T}}C)^{-1}C^{\mathrm{T}}(x_k - \overline{x}) = C^{\mathrm{T}}(x_k - \overline{x})$. Then, the method that we investigate minimizes (in that subspace) the volume of the resulting simplex such that it encloses the scores z_k of the observed bands of the pixels x_k.

B. Principle of MVES

The problem of finding the MVES of a set of points $z_k, k = 1, \ldots, r$ in $(n-1)$-dimensional space can be written as a so-called nonlinear optimization problem [46] with $(n-1) \times n$

variables $\hat{v}_{ij}$ and $n \times r$ constraints (nonnegativity) α_{jk} as follows:

$$\min_{\hat{V}} \left\{ f(\hat{V}) := \left| \det \begin{pmatrix} \hat{V} \\ \mathbf{1}^{\mathrm{T}} \end{pmatrix} \right| \right\}$$
$$\text{subject to :} \quad \alpha_k = \begin{pmatrix} \hat{V} \\ \mathbf{1}^{\mathrm{T}} \end{pmatrix}^{-1} \begin{pmatrix} z_k \\ 1 \end{pmatrix} \geq 0$$
$$k = 1, \ldots, r \tag{5}$$

where $\mathbf{1}$ is the all-one vector. It is worth noting that the same problem was formulated differently in [40] and [44]. Here, problem (5) is written down from a nonlinear optimization perspective, where nonnegativity and sum-to-one constraints are explicitly defined in the expressions. General nonlinear optimization codes (such as Matlab's `fmincon` function used in this work, `conopt`, `minos`, etc. [47]) are available to generate an optimum solution for the problem (5) giving a starting matrix V. They also provide information on the binding constraints which, in this specific problem, determine which α_{jk} has a value of zero and, therefore, which pixels k are active, i.e., they can be found on the boundary of simplex $\mathrm{conv}(\hat{V})$. In [46], it is shown that this is a global optimization problem, i.e., there are instances in which the problem has several local (nonglobal) solutions. However, in all cases of applying a nonlinear optimization algorithm to an instance of spectral unmixing, the optimum found has been a global minimum point. The initial matrix determines which of the minimum points (permutation of vertices) are found. Hendrix *et al.* [46] also describe the underlying combinatorial optimization problem aimed at by the N-FINDR algorithm [4]; the volume of the simplex is maximized (instead of minimized) by selecting n pixels out of r.

As discussed before, problem (5) generates the exact endmember matrix V in case all z_k's are convex combinations of its columns and there is no noise. In practice, there is noise and pixels z_k with an abundance of $a_{jk} = 0$ in model (3) may be located outside $S = \mathrm{conv}(V)$. As simplex $\hat{S} = \mathrm{conv}(\hat{V})$ includes all z_k's, it is usually larger in volume than the simplex S that we actually intend to estimate.

It should be noted that, in the specific case of remotely sensed hyperspectral data, noise is generally low due to the very high signal-to-noise ratio (SNR) achieved by instruments such as AVIRIS [2]. In addition, pixels are generally well spread on the boundary of the originating simplex, i.e., the high-dimensional space defined by the hyperspectral data is mostly empty, with most of the samples concentrated at the boundaries of S and at the corners [48]. Finally, it is known that, in practice, a mixed pixel consists of at most four to five constituents [6], [49]. These observations are all quite important in this context because, as soon as noise is added, one can approximate with the probability theory the chance that a pixel lays outside S.

C. Counting Interior and Exterior Points

Following model (3), it is desirable to estimate how many of the projected pixels z_k lay outside the simplex S. Given endmember matrix V, linear constrained (sum-to-one) unmixing of (3) results into an abundance estimator

$$\hat{a} = \begin{pmatrix} V \\ \mathbf{1}^{\mathrm{T}} \end{pmatrix}^{-1} \begin{pmatrix} z \\ 1 \end{pmatrix} = a + \begin{pmatrix} V \\ \mathbf{1}^{\mathrm{T}} \end{pmatrix}^{-1} \begin{pmatrix} \xi \\ 0 \end{pmatrix}. \tag{6}$$

Here, vector $\hat{a}$ has a normal distribution with mean a. The probability that a pixel lays within S is the probability that $\hat{a}$ is nonnegative, i.e., the probability mass of random variable $\hat{a}$ on the positive orthant. This exact probability is unpractical to work with. The following reasoning gives a crude approximation to the number of interior points which will be shown to be effective in practice. Let $a_j = 0$ for a pixel. As $\hat{a}_j$ is symmetric around zero, the probability that abundance value $\hat{a}_j$ is negative is one-half. Notice that the components of $\hat{a}$ are not stochastically independent. Let N represent the number of abundance values of a pixel that are zero, $N = 0, 1, \ldots, n-1$. The probability that the observation $\hat{a}$ of the pixel is inside the simplex S is approximated by $p_N = (1/2)^n$. Notice that we are dealing with the fact that low values of a_j may yield observations outside S. Therefore, it is relevant that, in practice, noise is relatively low and positive abundance estimates are obtained. The number P of observations z_k located inside simplex S that we want to estimate depends on the distribution of zero abundance values over the pixels. Let r_N denote the number of pixels that have N zero values such that $\sum r_N = r$. The number of pixels inside S is estimated by

$$P = \sum_{N=0}^{n-1} r_N p_N. \tag{7}$$

It is important to notice that, in an experimental setting using synthetic data, the number r_N is given by the construction of the data. In other experiments, the abundance estimation results obtained after using other endmember extraction methods can provide approximations of either r_N or P.

D. Algorithmic Description: Endmember Extraction

As suggested in the previous section, the relevance of P is that outer approximations $\hat{S}$ of S should in fact ignore the $r - P$ pixels outside S and enclose the P pixels that are located in S. Now, the question is how to determine which ones are inside S and which ones are outside. This consideration is the basis of a new estimation algorithm, called MINVEST and described in Algorithm 1. The idea is to base the final estimate of endmembers on the P pixels that are expected to be interior with respect to S. Iteratively, the endmembers are estimated from the minimum-volume problem (5), and the pixels at its boundary (i.e., those which have at least one $\alpha_j = 0$) are removed until P is left over. As starting simplex, one can take a random matrix or, for instance, the abundance estimation result after applying another algorithm such as N-FINDR. At this point, it is important to emphasize that such initialization (according to our experiments) mainly affects the computational efficiency of the algorithm but not the final obtained result.

After obtaining the estimate $\hat{V}$ of the endmembers, we can estimate the abundance of all pixels. Corresponding to $\hat{V}$, we have for pixel z

$$\hat{a} = \begin{pmatrix} \hat{V} \\ \mathbf{1}^{\mathrm{T}} \end{pmatrix}^{-1} \begin{pmatrix} z \\ 1 \end{pmatrix}. \tag{8}$$

The pixels located in the final set $Z0$ (geometrically within simplex $\hat{S}$) have automatically nonnegative abundance values corresponding to α_k in (5). A remaining question at this point is how to estimate the abundance for pixels outside $\hat{S}$.

Algorithm 1: MINVEST

Inputs: Z: $(n-1) \times r$ matrix of pixel scores
P: number of interior pixels
Output: $\hat{V}$: $(n-1) \times n$ matrix of endmember estimates
Funct MinVol estimator

1) Initialization: $R := r$, $Z0 := Z$, generate starting simplex $\hat{V}$
2) **while**$(R > P)$
3) Generate $\hat{V}$ by solving (5) for $Z0$, former $\hat{V}$ is starting value
4) remove pixels at boundary $\hat{S} = \mathrm{conv}(\hat{V})$ from $Z0$, update number of pixels to $R = |Z0|$
5) **endwhile**

E. Algorithmic Description: Abundance Estimation

Let us assume that pixel z is outside $\hat{S}$. In this case, the pixel has at least one $a_j < 0$. Now, we can use the idea that the noise ξ of z_k is component-wise independent by projecting z on the linear space of the facet of $\hat{S}$ close to z_k. Let $\mathbb{F}$ be the space of a facet containing $p \leq n$ vertices called $u_1, \ldots, u_p$. If we define matrix $W = [w_1, \ldots, w_{p-1}]$ with $w_j = u_j - u_p$, we can now write

$$\begin{aligned} \mathbb{F} &= \left\{ y = \sum_{j=1}^{p} a_j u_j | \sum_{j=1}^{p} a_j = 1 \right\} \\ &= \left\{ y = u_p + \sum_{j=1}^{p-1} d_j w_j | d \in \mathbb{R}^{p-1} \right\} = u_p + \langle W \rangle. \end{aligned} \tag{9}$$

The relation between the two representations is that, for an abundance a having $\sum_{j=1}^{p} a_j = 1 \rightarrow a_p = 1 - \sum_{j=1}^{p-1} a_j$, one can express the corresponding point $y \in \mathbb{F}$ as

$$y = \sum_{j=1}^{p} a_j u_j = u_p + \sum_{j=1}^{p-1} a_j (u_j - u_p) = u_p + \sum_{j=1}^{p-1} a_j w_j. \tag{10}$$

The projection of z on $\mathbb{F}$ implies finding y being the minimum point of

$$\min_{y \in \mathbb{F}} \|z - y\|^2 = \min_{a \in \mathbb{R}^{p-1}} \|z - u_p - Wa\|^2 \tag{11}$$

with minimum point $y = W(W^{\mathrm{T}}W)^{-1}W^{\mathrm{T}}(z - u_p)$ and corresponding abundance

$$\begin{aligned} a &= (W^{\mathrm{T}}W)^{-1}W^{\mathrm{T}}(z - u_p) \\ a &\in \mathbb{R}^{p-1} \text{ and } a_p = 1 - \sum_{j=1}^{p-1} a_j. \end{aligned} \tag{12}$$

An important choice to make at this point is which facet to project on, i.e., which a_j's are zero and, correspondingly, their v_j is not considered in matrix U. Let $\mathbb{J}(a) = \{j | a_j > 0\}$ be the index set of positive values in a vector a. Algorithm 2 first determines a via (8), then selects the endmembers v_j from $\mathbb{J}(a)$ into matrix U, determines W, and finally calculates (12). Although not often, it may occur that the result still contains negative components. In this case, those components can be set to zero, and (12) can be recalculated for the lower dimensional facet until only positive abundance values are left.

Algorithm 2: Abundance estimation

Inputs: V: $(n-1) \times n$ matrix of endmember scores
z: $n-1$ vector of pixel scores
Outputs: a: nonnegative abundance vector
Funct Abundance

1) Initialization: determine a via (8)
2) **while** not all components $(a_j \geq 0)$
3) for all j with $a_j < 0$, put $a_j := 0$
4) for all $j \in \mathbb{J}(a)$, put their v_j in U
5) Construct W and determine values a_j for $j \in \mathbb{J}(a)$ via (12)
6) **endwhile**

III. Experimental Results

A. Synthetic Hyperspectral Data

A database of five 100×100-pixel synthetic hyperspectral scenes has been created using fractals to generate distinct spatial patterns, which are then used to simulate linear mixtures of a set of endmember signatures selected from a spectral library compiled by the U.S. Geological Survey (USGS)[1] and made up of a total of 420 spectral signatures. The leftmost part of Fig. 2 displays the five fractal images used in the simulations. These images are further divided into a number of clusters using the k-means algorithm in [50], where the number of clusters extracted from the five fractal images was always larger than the number of endmember signatures, fixed in our experiments to $n = 9$. The resulting clusters are displayed in the rightmost part of Fig. 2. A crucial step in the simulation procedure is how to assign a spectral signature to each cluster. For this purpose, we have implemented an automatic procedure that follows a simple strategy, in which the $n = 9$ signatures are first assigned to spatially disjoint regions belonging to different clusters. The remaining regions are then assigned with

[1] http://speclab.cr.usgs.gov/spectral-lib.html

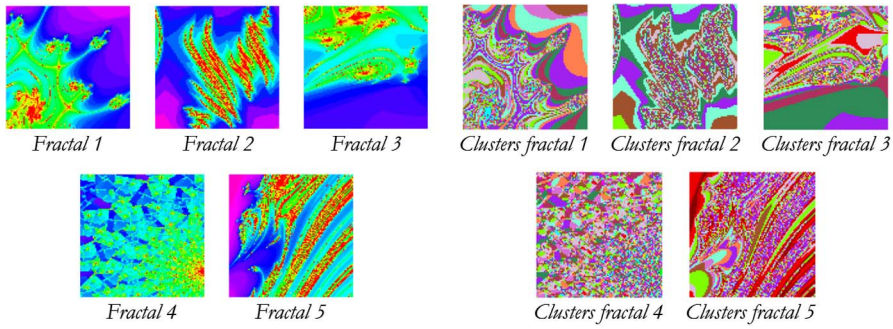

Fig. 2. Synthetic images used in experiments, where spatial patterns were generated using (left) fractals and then segmented into (right) clusters.

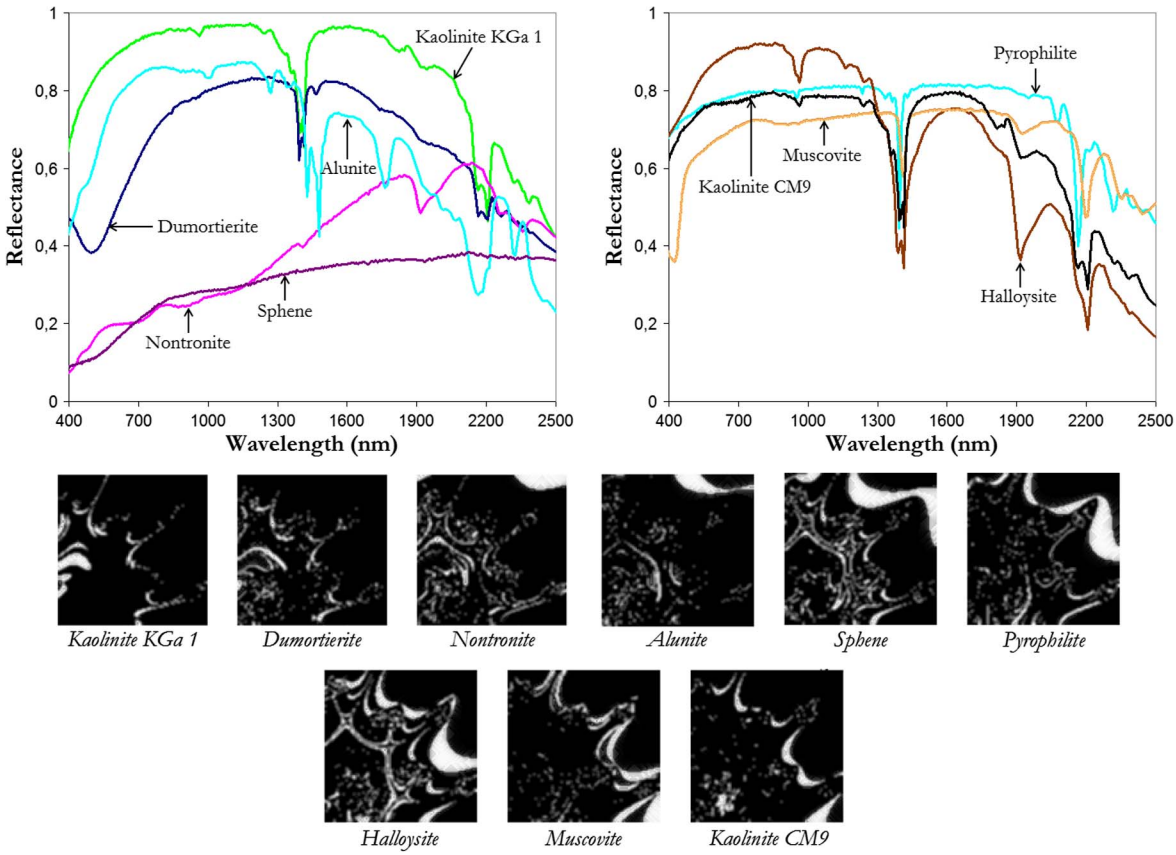

Fig. 3. (Top) USGS library signatures and (bottom) fractional abundance distributions considered for generating the simulated hyperspectral scene labeled as "Fractal 1" in experiments.

spectral signatures in an automatic way, ensuring the following: 1) Spatially disjoint regions are associated with different signatures, and 2) there is a balance in the overall number of pixels in the image which are associated to each spectral signature. Inside each region, the abundance proportions of spectral signatures have been simulated following a procedure that tries to imitate reality as much as possible, i.e., those pixels closer to the borders of the regions are more heavily mixed, while the pixels located at the center of the regions are more spectrally pure in nature. For this purpose, a Gaussian filter is applied, where the width of the Gaussian is carefully adjusted according to the width of each window. With the aforementioned procedure, the simulated regions exhibit the following properties.

1) All the simulated pixels inside a region are mixed, and the simulated image does not contain completely pure pixels. This increases the complexity of the unmixing problem and simulates the situation often encountered in real-world analysis scenarios, in which completely pure pixels are very rarely found.
2) The pixels close to the borders of the region are more heavily mixed than those in the center of the region.

TABLE I
AVERAGE SPECTRAL SIMILARITY SCORES (IN DEGREES) BETWEEN THE USGS MINERAL SPECTRA AND THEIR CORRESPONDING ENDMEMBER PIXELS PRODUCED BY SEVERAL ENDMEMBER EXTRACTION ALGORITHMS ACROSS THE FIVE SYNTHETIC SCENES IN FIG. 2

Algorithm	SNR=30:1	SNR=50:1	SNR=70:1	SNR=90:1	SNR=110:1	SNR= ∞
N-FINDR	2.089	0.464	0.384	0.389	0.362	0.362
OSP	2.118	0.452	0.350	0.361	0.345	0.364
VCA	2.188	0.520	0.368	0.434	0.436	0.400
SPP-N-FINDR	2.293	0.779	0.701	0.694	0.694	0.694
SPP-OSP	2.343	0.622	0.537	0.530	0.529	0.529
SPP-VCA	2.271	**0.456**	0.327	0.319	0.347	0.325
RBSPP-N-FINDR	2.175	0.875	0.676	0.787	0.804	0.785
RBSPP-OSP	2.227	0.764	1.021	1.089	1.034	0.898
RBSPP-VCA	**1.033**	0.686	0.678	0.809	0.715	0.669
AMEE	2.671	1.261	0.970	1.193	1.252	1.175
SSEE	2.125	1.078	0.576	0.723	0.646	0.475
MVSA	15.256	1.365	**0.130**	**0.028**	**0.024**	**0.024**
MVES	12.569	1.436	0.279	0.085	0.042	0.108
MINVEST	7.477	1.221	0.228	0.149	0.164	0.162

TABLE II
AVERAGE RMSE SCORES AFTER RECONSTRUCTING THE FIVE SYNTHETIC SCENES IN FIG. 2 USING THE ENDMEMBERS EXTRACTED BY SEVERAL METHODS

Algorithm	SNR=30:1	SNR=50:1	SNR=70:1	SNR=90:1	SNR=110:1	SNR= ∞
N-FINDR	0.356336	0.039180	0.009510	0.007453	0.008028	0.008029
OSP	0.359041	0.039359	0.010022	0.008277	0.008843	0.009067
VCA	0.369223	0.044585	0.017149	0.021748	0.018675	0.010606
SPP-N-FINDR	0.359943	0.045030	0.017994	0.016252	0.016202	0.016201
SPP-OSP	0.368326	0.048540	0.016941	0.015210	0.015159	0.015158
SPP-VCA	0.368823	0.040922	0.011250	0.009823	0.009000	0.007831
RBSPP-N-FINDR	0.358208	0.049320	0.028065	0.026850	0.028388	0.026568
RBSPP-OSP	0.359748	0.055439	0.072980	0.054676	0.054219	0.043830
RBSPP-VCA	0.308590	0.048593	0.033052	0.043469	0.028862	0.025272
AMEE	0.627502	0.484898	0.468297	0.473804	0.484930	0.491231
SSEE	0.358918	0.135952	0.035355	0.066931	0.026965	0.046549
MVSA	**0.296320**	**0.029640**	**0.002980**	**0.000513**	**0.000418**	**0.000418**
MVES	0.296900	0.029720	0.003000	0.000514	0.000420	0.000419
MINVEST	0.298320	0.036460	0.004140	0.000858	0.000820	0.000800

3) If the simulated region is sufficiently large, the pixels located at the center can exhibit a degree of purity of 99% of a certain endmember. However, if the size of the simulated region is small, the degree of purity of pixels at the center of the region can decrease until 95% of a certain endmember, while pixels located in the region borders are generally much more heavily mixed.

To conclude the simulation process, zero-mean Gaussian noise was added to the scenes in different SNRs—from 30 : 1 to 110 : 1—to simulate contributions from ambient and instrumental sources. The procedure used to simulate different SNR values in our experiments is the one described in [13]. For illustrative purposes, Fig. 3 shows the spectra of the USGS signatures used in the simulation of one of the synthetic scenes (the one labeled as "Fractal 1" in Fig. 2). All the simulated scenes are available online.[2] The abundance maps associated to each reference USGS signature in the construction of the synthetic scene are also shown in Fig. 3, where the black color indicates 0% abundance of the corresponding mineral, the white color indicates 100% abundance of the mineral, and the fractional abundances in each pixel of the scene sum to unity, thus ensuring that the simulated fractal images strictly adhere to a fully constrained linear mixture model.

Several different metrics have been used to measure the performance of endmember identification and spectral unmixing algorithms in the synthetic fractal scenes. The first metric is the spectral angle (SA) [51] between each extracted endmember

[2]http://www.umbc.edu/rssipl/people/aplaza/fractals.zip

TABLE III
AVERAGE RMSE SCORES BETWEEN THE GROUND-TRUTH AND THE ESTIMATED ABUNDANCE MAPS ACROSS THE FIVE SYNTHETIC SCENES IN FIG. 2 FOR THE ENDMEMBER IDENTIFICATION METHODS WITHOUT THE PURE PIXEL ASSUMPTION

Algorithm	SNR=30:1	SNR=50:1	SNR=70:1	SNR=90:1	SNR=110:1	SNR= ∞
MVSA	0.111385	**0.021149**	**0.002337**	**0.000432**	**0.000356**	**0.000211**
MVES	0.114632	0.026371	0.008103	0.001695	0.000996	0.000347
MINVEST	**0.090770**	0.034890	0.006671	0.005447	0.006926	0.006782

TABLE IV
AVERAGE RMSE SCORES BETWEEN THE GROUND-TRUTH ENDMEMBERS AND THE ENDMEMBER SIGNATURES IDENTIFIED BY ALGORITHMS WITHOUT THE PURE PIXEL ASSUMPTION ACROSS THE FIVE SYNTHETIC SCENES IN FIG. 2

Algorithm	SNR=30:1	SNR=50:1	SNR=70:1	SNR=90:1	SNR=110:1	SNR= ∞
MVSA	0.159665	0.018010	**0.001808**	**0.000366**	**0.000311**	**0.000131**
MVES	0.146744	0.020800	0.004128	0.001099	0.000520	0.000302
MINVEST	**0.092180**	**0.015617**	0.003691	0.002686	0.002624	0.002601

TABLE V
NUMBER OF INTERIOR PIXELS P FOR EACH OF THE FIVE SYNTHETIC SCENES IN FIG. 2

Fractal 1	Fractal 2	Fractal 3	Fractal 4	Fractal 5
311	291	305	545	550

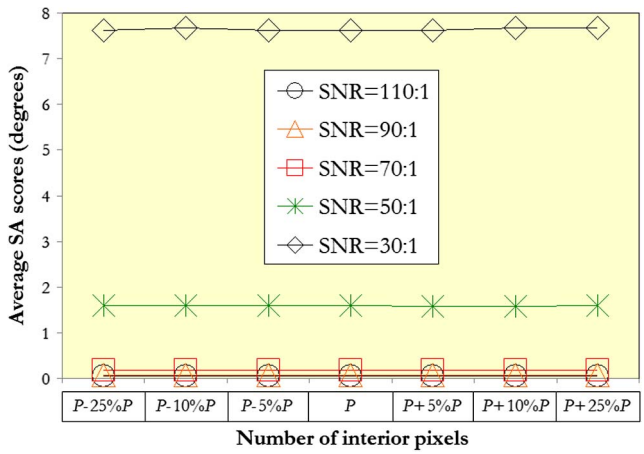

Fig. 4. Analysis of the sensitivity of MINVEST to the number of interior pixels using the average SA (across the five synthetic scenes in Fig. 2) as the performance metric.

TABLE VI
RMSE SCORES AFTER RECONSTRUCTING THE AVIRIS CUPRITE IMAGE USING THE ENDMEMBERS EXTRACTED BY SEVERAL METHODS

Algorithm	Average RMSE
N-FINDR	0.1068
OSP	0.4184
VCA	0.1007
SPP-N-FINDR	0.0951
SPP-OSP	0.1248
SPP-VCA	0.2229
RBSPP-N-FINDR	0.1024
RBSPP-OSP	0.1416
RBSPP-VCA	0.1065
AMEE	0.1916
SSEE	0.1272
MVSA	0.0389
MVES	0.0392
MINVEST	0.0393

and the set of available USGS ground-truth spectral signatures. Low SA scores mean high spectral similarity between the compared vectors (the value range of SA is [0, 90] degrees). This spectral similarity measure is invariant under the multiplication of pixel vectors by constants and, consequently, is invariant to unknown multiplicative scaling that may arise due to differences in illumination. The SA allows identification of the USGS signature most similar to each endmember by looking for the minimum SA distance between the endmember and USGS signature among the entire set.

The second metric to evaluate the goodness of the reconstruction is the root-mean-square error (rmse) between the original and the reconstructed hyperspectral scene [16]. Let $\mathbf{I}$ be the synthetic hyperspectral scene and $\hat{\mathbf{I}}$ be a reconstructed version of $\mathbf{I}$. Specifically, the pixel vector at spatial coordinates (i, j) in the original hyperspectral scene is $\mathbf{I}(i,j) = [x_1(i,j), x_2(i,j), \ldots, x_m(i,j)]$, and the corresponding pixel vector at the same spatial coordinates in the reconstructed hyperspectral scene is $\hat{\mathbf{I}}(i,j) = [\hat{x}_1(i,j), \hat{x}_2(i,j), \ldots, \hat{x}_m(i,j)]$. The rmse between the original and reconstructed hyperspectral scenes is calculated as follows:

$$\text{rmse}(\mathbf{I}, \hat{\mathbf{I}}) = \frac{1}{s \times l} \sum_{i=1}^{s} \sum_{j=1}^{l} \left(\frac{1}{m} \sum_{k=1}^{m} (x_k(i,j) - \hat{x}_k(i,j))^2 \right)^{\frac{1}{2}} \tag{13}$$

where $s \times l$ is the number of pixels in the hyperspectral image. It should be noted that the rmse metric is based on the assumption that a set of high-quality endmembers may allow reconstruction of the synthetic hyperspectral scene with higher precision than a set of low-quality endmembers, regardless of the presence of such endmembers in the original scene. Finally, other performance metrics used in our experiments with synthetic scenes are the rmse between the ground-truth

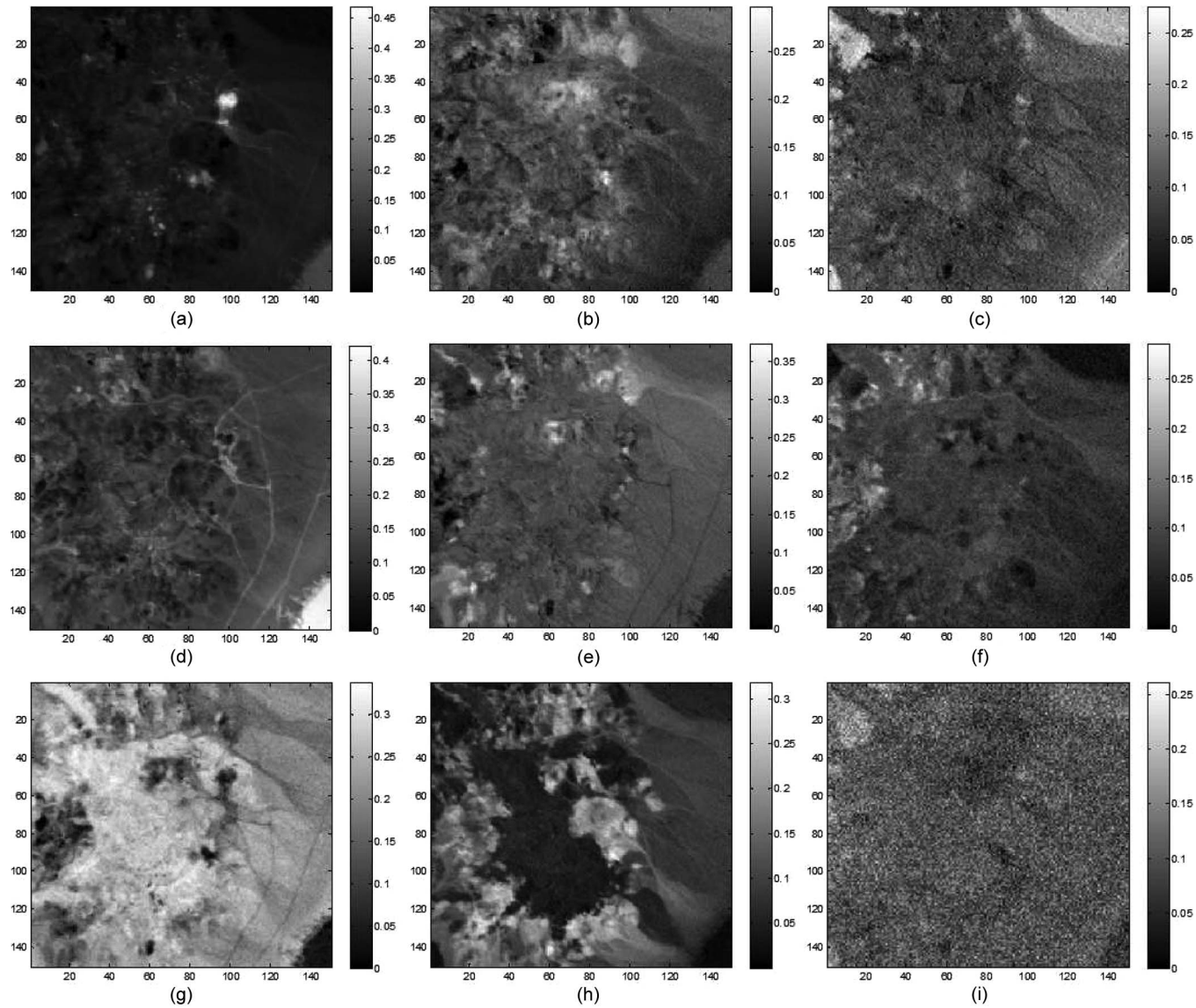

Fig. 5. Fractional abundance maps obtained for the AVIRIS Cuprite image by MVSA.

abundance maps and the abundances estimated after applying the different endmember identification methods, and the rmse between the ground-truth endmembers and the endmember signatures identified by different methods.

The algorithms selected for comparative purposes comprise three spectral-based techniques which assume the presence of pure pixels in the scene (N-FINDR [4], OSP [13], and VCA [14]), an SPP technique which can be combined with spectral-based algorithms designed under the pure pixel assumption (SPP [16]), an RBSPP technique which can also be combined with spectral-based algorithms (RBSPP [17]), two spatial–spectral techniques based on the pure pixel assumption (AMEE [15] and SSEE [52]); two endmember identification algorithms which do not assume the presence of pure pixels in the input scene (MVSA [39] and MVES [41]), and the presented MINVEST algorithm. For the nonlinear optimization in MINVEST, the `fmincon` solver of Matlab 7.5.0342 (R2007b) was used. Matlab codes of both MVSA and MVES have been provided by the algorithm developers. The other algorithms have been implemented according to the original descriptions available in the literature.

Table I shows the average spectral similarity scores (in degrees) between the reference USGS mineral spectra and their corresponding endmember pixels produced by the endmember identification algorithms, across the five synthetic scenes in Fig. 2. As a result, each value in Table I is the average SA obtained after processing the five considered scenes with the same SNR (five different SNR values, ranging from $30:1$ to $110:1$, are reported in the table). Numerical results from Table I show that, for SNR $> 50:1$, algorithms which do not assume the existence of pure pixels outperform those assuming the presence of pure pixels in the hyperspectral image. However, for noisy data (SNR $<= 50:1$, which is far away from current sensor specifications in terms of SNR [2]), methods based on SPP perform better. As shown in Table I, for low SNR values, all methods which do not assume the presence of pure pixels in the data exhibit poor performance in terms of the SA.

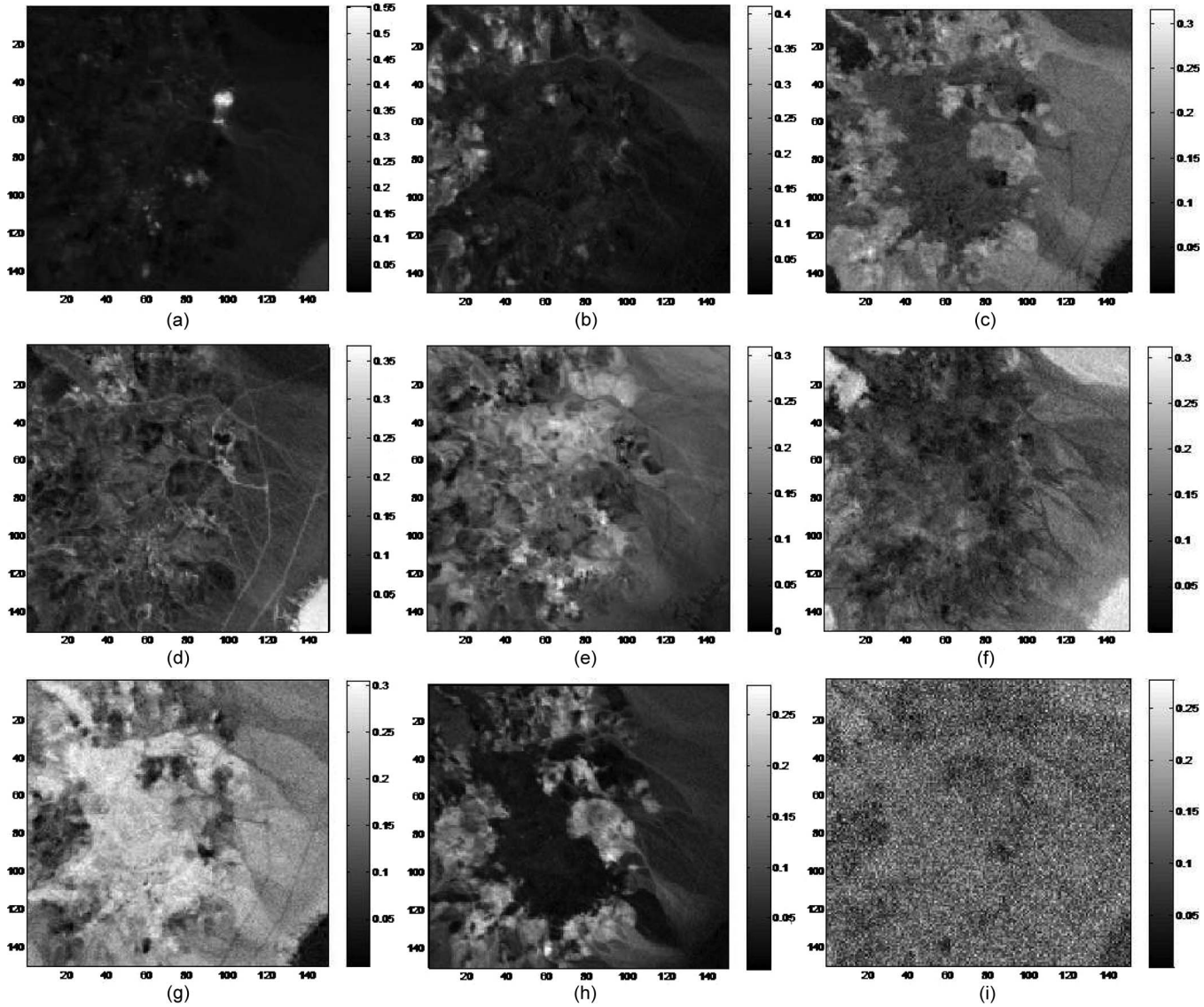

Fig. 6. Fractional abundance maps obtained for the AVIRIS Cuprite image by MVES.

On the other hand, Table II reports the reconstruction rmse between the original and the reconstructed versions of the synthetic scenes in Fig. 2, obtained using the endmembers extracted by several methods. As show in Table II, the methods without the pure pixel assumption outperform those methods which assume the existence of pure pixels, even in noisy analysis scenarios. In order to further substantiate the performance of endmember identification algorithms without the pure pixel assumption, Table III shows the rmse between the ground-truth and the estimated abundance maps obtained for these methods, while Table IV shows the rmse between the ground-truth endmembers and the endmember signatures identified by the same methods. As shown in Table III, MINVEST can only outperform the other tested methods in low SNR conditions $(\text{SNR} <= 30:1)$, while for the other SNR cases, MVSA provides the best scores of rmse in abundance estimation. On the other hand, Table IV provides similar observations, with MINVEST outperforming the other tested methods for $\text{SNR} <= 50:1$.

At this point, it is important to emphasize that we have also analyzed the statistical significance of the improvements achieved by the algorithms without the pure pixel assumption (in terms of the considered performance metrics) by repeating the random noise generation step 50 times for each simulated fractal scene and SNR level and calculated the mean values (reported in Tables II–IV) and the standard deviation of the obtained results. The standard deviations, which do not vary significantly for the different tested methods, are not displayed in the tables for better visualization of the results. However, we have observed that the standard deviation in the measured values across the 50 runs is always at least 10 times smaller than the mean value. This indicates that the measured values for all the considered metrics do not deviate significantly from their mean; hence, the reported improvements can be considered statistically significant.

To conclude this section, we describe an experiment analyzing the sensitivity of MINVEST to the number of interior pixels P, which is an input parameter for the algorithm. Table V

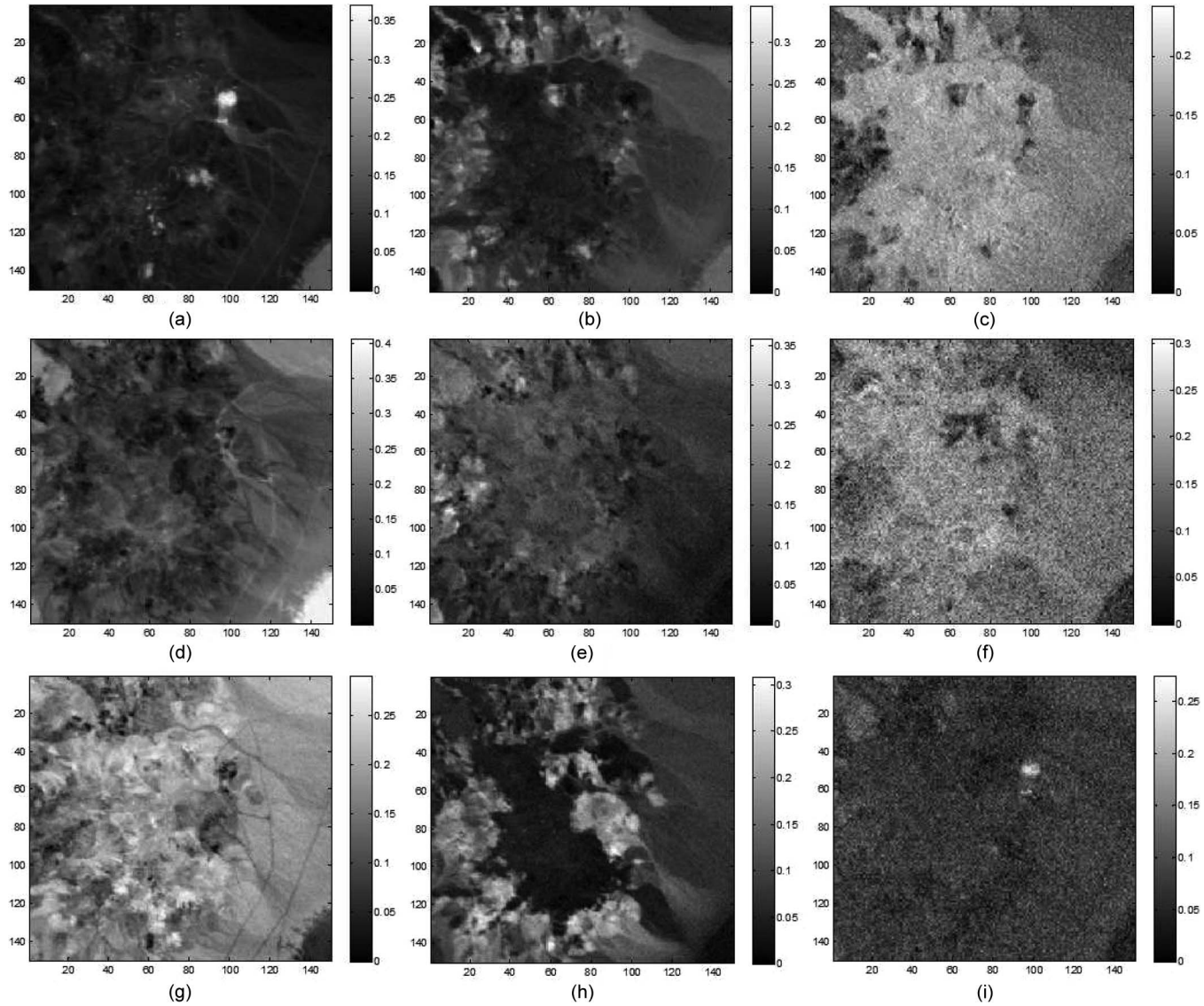

Fig. 7. Fractional abundance maps obtained for the AVIRIS Cuprite image by MINVEST.

shows the estimated values of P for each of the five synthetic hyperspectral images considered in our experiments. It should be noted that, for each synthetic data set, the distribution r_N is known from the ground truth and can be used to derive an estimate of P. On the other hand, Fig. 4 shows the plot of the average spectral similarity scores obtained by MINVEST for the synthetic scenes when the number of interior pixels was set to the optimal value (denoted by P in Fig. 4) and to values that deviate 5%, 10%, and 25% above or below such optimal value. As indicated in Fig. 4, the average SA scores remain almost identical for all considered SNR values regardless of the choice of the number of interior pixels. This experiment indicates that the final estimation is not sensitive to the actual value of P, i.e., removing or not removing many points hardly influences the resulting simplex if data are well spread. Similar results were obtained for the other considered performance metrics, and therefore, these results are not reported here for space considerations.

B. Real Hyperspectral Data

This experiment uses the well-known AVIRIS Cuprite data set, available online in reflectance units[3] after atmospheric correction. This scene has been widely used to investigate the performance of endmember extraction algorithms. The portion used in experiments corresponds to a 150 $\times$ 150-pixel subset of the sector labeled as f970619t01p02_r02_sc03.a.rfl in the online data. The scene comprises 224 spectral bands between 0.4 and 2.5 μm, with full-width at half-maximum of 10 nm and spatial resolution of 20 m per pixel. Prior to the analysis, several bands were removed due to water absorption and low SNR in those bands, leaving a total of 192 reflectance channels to be used in the experiments. The Cuprite site is well understood mineralogically [53], [54] and has several exposed

[3]http://aviris.jpl.nasa.gov/html/aviris.freedata.html

minerals of interest included in a spectral library compiled by the USGS.[4]

Table VI shows the rmse scores after reconstructing the AVIRIS Cuprite image using the endmembers extracted by different methods. In all cases, the number of endmembers was set to $n = 9$ using the virtual dimensionality concept [6]. For the MINVEST method, the value for the number of interior pixels was set empirically to $P = 2810$ from the distribution of zeros over the pixels after analyzing the outcome of the N-FINDR algorithm applied to the data. The tendency of the results is similar to that of the experiments with synthetic scenes; the algorithms which assume the presence of pure pixels in the image provide higher reconstruction errors than the three considered algorithms without the pure pixel assumption, which provide similar results.

Figs. 5–7 show the fully constrained fractional abundance maps estimated by MVSA, MVES, and MINVEST, respectively. Compared to the published geologic maps [55], these estimations present a high level of similarity. Given the spatial resolution of 20 m per pixel, it is reasonable to assume that most of the pixels in the AVIRIS Cuprite scene are made up of several different constituents. In this regard, the fractional abundance estimations provided by MVSA, MVES, and MINVEST seem realistic since most of the mineral maps do not indicate the presence of completely pure instances of minerals across the pixels of the scene. A visual assessment of the maps in Figs. 5–7 reveals that some endmembers are well identified by all methods, for instance, the maps labeled as (a) correspond to the buddingtonite mineral, which appears in the image as an anomaly, while the maps labeled as (d) correspond to a spatially homogeneous area: the *montmorillonite* playa, located at the lower rightmost corner of the scene.

IV. Conclusions and Future Research Lines

In this paper, a novel endmember identification algorithm (of minimum-volume enclosing type) has been presented and analyzed. The main features of the algorithm are as follows: 1) It does not require pure samples to be present in the input hyperspectral data; 2) it is based on iteratively removing pixels from an enclosing simplex expected to be outside the ground-truth simplex; and 3) it incorporates the fractional abundance estimation as an internal step of the endmember searching process itself. The performance of the algorithm has been evaluated using synthetic and real hyperspectral scenes and compared to other state-of-the-art endmember identification algorithms. Analyses with synthetic data indicate that the described method is effective in the characterization of constituents that never appear in pure form in the scene. These experiments also reveal that the method outperforms algorithms designed under the pure pixel assumption and provides comparable results with regard to other algorithms which do not assume the presence of pure pixels in the scene. The analyses with real hyperspectral data reveal similar conclusions and further indicate that the described new method has the potential to outperform other endmember identification algorithms with and without the pure pixel assumption in real analysis scenarios. This flexible and adaptive behavior broadens the application domain with regard to other methods which exhibit more restrictions than the presented one, such as the need for pure instances of each endmember to be present in the input data or the need to resort to an external method to produce endmember fractional abundances (the final product in spectral unmixing applications).

As with any new approach, there are some unresolved issues that may present challenges over time. One of them is estimating the number P of interior pixels on which the final result is based. In this paper, the value could be based on the result of other methods. Although our experimental results indicate that the method is not very sensitive to the setting of this parameter, a more detailed investigation of automatic procedures in order to set the optimal value for this parameter after observing the input data properties is worth being conducted in future research. Another issue to be addressed in future developments is the computational complexity of the algorithm, which, in any event, is similar to that exhibited by other endmember identification methods of the same type, such as MVSA or MVES. Although the experimental results reported in this paper are encouraging, further experiments with additional hyperspectral scenes and endmember identification methods should be conducted in future research to fully substantiate these remarks.

[4]http://speclab.cr.usgs.gov/spectral-lib.html

Acknowledgment

The author E. M. T. Hendrix is a Fellow of the Spanish "Ramon y Cajal" Program cofinanced by the European Social Fund. The authors would like to thank the Associate Editor and the three anonymous reviewers for the outstanding comments and suggestions, which greatly helped them to improve the technical quality and presentation of this manuscript.

References

[1] A. Plaza, J. A. Benediktsson, J. Boardman, J. Brazile, L. Bruzzone, G. Camps-Valls, J. Chanussot, M. Fauvel, P. Gamba, J. Gualtieri, M. Marconcini, J. C. Tilton, and G. Trianni, "Recent advances in techniques for hyperspectral image processing," *Remote Sens. Environ.*, vol. 113, pp. 110–122, Sep. 2009.

[2] R. O. Green, M. L. Eastwood, C. M. Sarture, T. G. Chrien, M. Aronsson, B. J. Chippendale, J. A. Faust, B. E. Pavri, C. J. Chovit, M. Solis, M. R. Olah, and O. Williams, "Imaging spectroscopy and the Airborne Visible/Infrared Imaging Spectrometer (AVIRIS)," *Remote Sens. Environ.*, vol. 65, no. 3, pp. 227–248, Sep. 1998.

[3] J. B. Adams, M. O. Smith, and P. E. Johnson, "Spectral mixture modeling: A new analysis of rock and soil types at the Viking Lander 1 site," *J. Geophys. Res.*, vol. 91, pp. 8098–8112, Jul. 1986.

[4] M. E. Winter, "N-FINDR: An algorithm for fast autonomous spectral end-member determination in hyperspectral data," in *Proc. SPIE Image Spectrom. V*, 2003, vol. 3753, pp. 266–277.

[5] D. Heinz and C.-I. Chang, "Fully constrained least squares linear mixture analysis for material quantification in hyperspectral imagery," *IEEE Trans. Geosci. Remote Sens.*, vol. 39, no. 3, pp. 529–545, Mar. 2001.

[6] C.-I. Chang and Q. Du, "Estimation of number of spectrally distinct signal sources in hyperspectral imagery," *IEEE Trans. Geosci. Remote Sens.*, vol. 42, no. 3, pp. 608–619, Mar. 2004.

[7] J. M. Bioucas-Dias and J. M. P. Nascimento, "Hyperspectral subspace identification," *IEEE Trans. Geosci. Remote Sens.*, vol. 46, no. 8, pp. 2435–2445, Aug. 2008.

[8] J. A. Richards and X. Jia, *Remote Sensing Digital Image Analysis: An Introduction*. New York: Springer-Verlag, 2006.

[9] A. A. Green, M. Berman, P. Switzer, and M. D. Craig, "A transformation for ordering multispectral data in terms of image quality with implications

for noise removal," *IEEE Trans. Geosci. Remote Sens.*, vol. 26, no. 1, pp. 65–74, Jan. 1988.
[10] A. Plaza, P. Martinez, R. Perez, and J. Plaza, "A quantitative and comparative analysis of endmember extraction algorithms from hyperspectral data," *IEEE Trans. Geosci. Remote Sens.*, vol. 42, no. 3, pp. 650–663, Mar. 2004.
[11] Q. Du, N. Raksuntorn, N. H. Younan, and R. L. King, "End-member extraction for hyperspectral image analysis," *Appl. Opt.*, vol. 47, no. 28, pp. 77–84, Oct. 2008.
[12] J. Chanussot, M. M. Crawford, and B.-C. Kuo, "Foreword to the special issue on hyperspectral image and signal processing," *IEEE Trans. Geosci. Remote Sens.*, vol. 48, no. 11, pp. 3871–3876, Nov. 2010.
[13] J. C. Harsanyi and C.-I. Chang, "Hyperspectral image classification and dimensionality reduction: An orthogonal subspace projection," *IEEE Trans. Geosci. Remote Sens.*, vol. 32, no. 4, pp. 779–785, Jul. 1994.
[14] J. M. P. Nascimento and J. M. Bioucas-Dias, "Vertex component analysis: A fast algorithm to unmix hyperspectral data," *IEEE Trans. Geosci. Remote Sens.*, vol. 43, no. 4, pp. 898–910, Apr. 2005.
[15] A. Plaza, P. Martinez, R. Perez, and J. Plaza, "Spatial/spectral endmember extraction by multidimensional morphological operations," *IEEE Trans. Geosci. Remote Sens.*, vol. 40, no. 9, pp. 2025–2041, Sep. 2002.
[16] M. Zortea and A. Plaza, "Spatial preprocessing for endmember extraction," *IEEE Trans. Geosci. Remote Sens.*, vol. 47, no. 8, pp. 2679–2693, Aug. 2009.
[17] G. Martin and A. Plaza, "Region-based spatial preprocessing for endmember extraction and spectral unmixing," *IEEE Geosci. Remote Sens. Lett.*, vol. 8, no. 4, pp. 745–749, Jul. 2011.
[18] O. Duran and M. Petrou, "Robust endmember extraction in the presence of anomalies," *IEEE Trans. Geosci. Remote Sens.*, vol. 49, no. 6, pp. 1986–1996, Jun. 2011.
[19] B. Zhang, X. Sun, L. Gao, and L. Yang, "Endmember extraction of hyperspectral remote sensing images based on the ant colony optimization (ACO) algorithm," *IEEE Trans. Geosci. Remote Sens.*, vol. 49, no. 7, pp. 2635–2646, Jul. 2011.
[20] M. Shoshany, F. Kizel, N. Netanyahu, N. Goldshlager, T. Jarmer, and G. Even-Tzur, "An iterative search in end-member fraction space for spectral unmixing," *IEEE Geosci. Remote Sens. Lett.*, vol. 8, no. 4, pp. 706–709, Jul. 2011.
[21] J. Silvan-Cardenas and L. Wang, "Fully constrained linear spectral unmixing: Analytic solution using fuzzy sets," *IEEE Trans. Geosci. Remote Sens.*, vol. 48, no. 11, pp. 3992–4002, Nov. 2010.
[22] C.-I. Chang, C.-C. Wu, and H.-M. Chen, "Random pixel purity index," *IEEE Geosci. Remote Sens. Lett.*, vol. 7, no. 2, pp. 324–328, Apr. 2010.
[23] F. Schmidt, A. Schmidt, E. Treandguier, M. Guiheneuf, S. Moussaoui, and N. Dobigeon, "Implementation strategies for hyperspectral unmixing using Bayesian source separation," *IEEE Trans. Geosci. Remote Sens.*, vol. 48, no. 11, pp. 4003–4013, Nov. 2010.
[24] A. Zare and P. Gader, "PCE: Piecewise convex endmember detection," *IEEE Trans. Geosci. Remote Sens.*, vol. 48, no. 6, pp. 2620–2632, Jun. 2010.
[25] S. Mei, M. He, Z. Wang, and D. Feng, "Spatial purity based endmember extraction for spectral mixture analysis," *IEEE Trans. Geosci. Remote Sens.*, vol. 48, no. 9, pp. 3434–3445, Sep. 2010.
[26] D. Thompson, L. Mandrake, M. Gilmore, and R. Castano, "Superpixel endmember detection," *IEEE Trans. Geosci. Remote Sens.*, vol. 48, no. 11, pp. 4023–4033, Nov. 2010.
[27] C.-I. Chang, C.-C. Wu, C.-S. Lo, and M.-L. Chang, "Real-time simplex growing algorithms for hyperspectral endmember extraction," *IEEE Trans. Geosci. Remote Sens.*, vol. 48, no. 4, pp. 1834–1850, Apr. 2010.
[28] M. Zortea and A. Plaza, "A quantitative and comparative analysis of different implementations of N-FINDR: A fast endmember extraction algorithm," *IEEE Geosci. Remote Sens. Lett.*, vol. 6, no. 4, pp. 787–791, Oct. 2009.
[29] S. Dowler and M. Andrews, "On the convergence of N-FINDR and related algorithms: To iterate or not to iterate?," *IEEE Geosci. Remote Sens. Lett.*, vol. 8, no. 1, pp. 4–8, Jan. 2011.
[30] X. Chen, J. Chen, X. Jia, B. Somers, J. Wu, and P. Coppin, "A quantitative analysis of virtual endmembers' increased impact on the collinearity effect in spectral unmixing," *IEEE Trans. Geosci. Remote Sens.*, vol. 49, no. 8, pp. 2945–2956, Aug. 2011.
[31] A. Ifarraguerri and C.-I. Chang, "Multispectral and hyperspectral image analysis with convex cones," *IEEE Trans. Geosci. Remote Sens.*, vol. 37, no. 2, pp. 756–770, Mar. 1999.
[32] M. Berman, H. Kiiveri, R. Lagerstrom, A. Ernst, R. Dunne, and J. F. Huntington, "ICE: A statistical approach to identifying endmembers in hyperspectral images," *IEEE Trans. Geosci. Remote Sens.*, vol. 42, no. 10, pp. 2085–2095, Oct. 2004.
[33] A. Zare and P. Gader, "Sparsity promoting iterated constrained endmember detection for hyperspectral imagery," *IEEE Geosci. Remote Sens. Lett.*, vol. 4, no. 3, pp. 446–450, Jul. 2007.
[34] J. M. P. Nascimento and J. M. Bioucas-Dias, "Dependent component analysis: A hyperspectral unmixing algorithm," in *Proc. IEEE Int. Geosci. Remote Sens. Symp.*, 2007, vol. 1, pp. 4033–4036.
[35] J. H. Bowles, P. J. Palmadesso, J. A. Antoniades, M. M. Baumback, and L. J. Rickard, "Use of filter vectors in hyperspectral data analysis," in *Proc. SPIE Infrared Spaceborne Remote Sens. III*, 1995, vol. 2553, pp. 148–157.
[36] M. T. Eismann and D. Stein, "Stochastic mixture modeling," in *Hyperspectral Data Exploitation: Theory and Applications*, C.-I. Chang, Ed. New York: Wiley, 2007.
[37] O. Eches, N. Dobigeon, C. Mailhes, and J.-Y. Tourneret, "Bayesian estimation of linear mixtures using the normal compositional model. Application to hyperspectral imagery," *IEEE Trans. Image Process.*, vol. 19, no. 6, pp. 1403–1413, Jun. 2010.
[38] M. D. Craig, "Minimum-volume transforms for remotely sensed data," *IEEE Trans. Geosci. Remote Sens.*, vol. 32, no. 3, pp. 542–552, May 1994.
[39] J. Li and J. Bioucas-Dias, "Minimum volume simplex analysis: A fast algorithm to unmix hyperspectral data," in *Proc. IEEE Int. Geosci. Remote Sens. Symp.*, 2008, vol. 3, pp. 250–253.
[40] T.-H. Chan, C.-Y. Chi, Y.-M. Huang, and W.-K. Ma, "A convex analysis-based minimum-volume enclosing simplex algorithm for hyperspectral unmixing," *IEEE Trans. Signal Process.*, vol. 57, no. 11, pp. 4418–4432, Nov. 2009.
[41] L. Miao and H. Qi, "Endmember extraction from highly mixed data using minimum volume constrained nonnegative matrix factorization," *IEEE Trans. Geosci. Remote Sens.*, vol. 45, no. 3, pp. 765–777, Mar. 2007.
[42] X. Liu, W. Xia, B. Wang, and L. Zhang, "An approach based on constrained nonnegative matrix factorization to unmix hyperspectral data," *IEEE Trans. Geosci. Remote Sens.*, vol. 49, no. 2, pp. 757–772, Feb. 2011.
[43] A. Huck, M. Guillaume, and J. Blanc-Talon, "Minimum dispersion constrained nonnegative matrix factorization to unmix hyperspectral data," *IEEE Trans. Geosci. Remote Sens.*, vol. 48, no. 6, pp. 2590–2602, Jun. 2010.
[44] T.-H. Chan, C.-Y. Chi, Y.-M. Huang, and W.-K. Ma, "Convex analysis based minimum-volume enclosing simplex algorithm for hyperspectral unmixing," in *Proc. IEEE Int. Conf. Acoust., Speech Signal Process.*, 2009, pp. 1089–1092.
[45] N. Dobigeon, S. Moussaoui, M. Coulon, J.-Y. Tourneret, and A. O. Hero, "Joint Bayesian endmember extraction and linear unmixing for hyperspectral imagery," *IEEE Trans. Signal Process.*, vol. 57, no. 11, pp. 4355–4368, Nov. 2009.
[46] E. M. T. Hendrix, I. García, J. Plaza, and A. Plaza, "Minimum volume simplicial enclosure for spectral unmixing," Mansholt Graduate School, Wageningen Univ., Wageningen, The Netherlands, Tech. Rep. MWP-50, 2010.
[47] E. M. T. Hendrix and B. G. Toth, *Introduction to Nonlinear and Global Optimization*. New York: Springer-Verlag, 2010.
[48] D. A. Landgrebe, *Signal Theory Methods in Multispectral Remote Sensing*. New York: John Wiley & Sons, 2003.
[49] R. A. Schowengerdt, *Remote Sensing: Models and Methods for Image Processing*., 2nd ed. New York: Academic, 1997.
[50] J. A. Hartigan and M. A. Wong, "Algorithm as 136: A *k*-means clustering algorithm," *J. Roy. Stat. Soc. Ser. C (Appl. Stat.)*, vol. 28, no. 1, pp. 100–108, 1979.
[51] N. Keshava and J. F. Mustard, "Spectral unmixing," *IEEE Signal Process. Mag.*, vol. 19, no. 1, pp. 44–57, Jan. 2002.
[52] D. M. Rogge, B. Rivard, J. Zhang, A. Sanchez, J. Harris, and J. Feng, "Integration of spatial–spectral information for the improved extraction of endmembers," *Remote Sens. Environ.*, vol. 110, no. 3, pp. 287–303, 2007.
[53] R. N. Clark, G. A. Swayze, K. E. Livo, R. F. Kokaly, S. J. Sutley, J. B. Dalton, R. R. McDougal, and C. A. Gent, "Imaging spectroscopy: Earth and planetary remote sensing with the USGS tetracorder and expert systems," *J. Geophys. Res.*, vol. 108, pp. 5131–44, Dec. 2003.
[54] G. Swayze, R. N. Clark, F. Kruse, S. Sutley, and A. Gallagher, "Ground-truthing AVIRIS mineral mapping at Cuprite, Nevada," in *Proc. JPL Airborne Earth Sci. Workshop*, 1992, pp. 47–49.
[55] G. Swayze, "The hydrothermal and structural history of the Cuprite mining district, Southwestern Nevada: An integrated geological and geophysical approach," Ph.D. dissertation, Univ. Colorado, Boulder, CO, 1997.

Eligius M. T. Hendrix received the B.S. and M.S. degrees in econometrics from Tilburg University, Tilburg, The Netherlands, in 1984 and 1987, respectively, and the Ph.D. degree from Wageningen University, Wageningen, The Netherlands, in 1998.

He was an Assistant Professor of operations research with the Mathematics and Social Science Department, Wageningen University, until 2005. After that, he was an Associate Professor of operations research with Wageningen University, and since 2008, he has been a Ramon y Cajal Researcher with the Department of Computer Architecture, University of Málaga. He is the Editor of the *Journal of Global Optimization*. His research interests include global optimization algorithms and its applications. He coauthored several books and articles in this area.

Inmaculada García received the B.Sc. degree in physics from the Complutense University of Madrid, Madrid, Spain, in 1977 and the Ph.D. degree from the University of Santiago de Compostela, Santiago de Compostela, Spain, in 1986.

She was with the University of Almeria, Almeria, Spain, where she was an Assistant Professor from 1977 to 1987, an Associate Professor during 1987–1997, and a Full Professor between 1997 and 2010. She was the Head of the Department of Computer Architecture and Electronics, University of Almeria, for more than 12 years. During 1994–1995, she was a Visiting Researcher at the University of Pennsylvania, Philadelphia. She has been the Head of the Supercomputing-Algorithms Research Group between 1990–2010. Since 2010, she has been a Full Professor with the University of Málaga. Her research interest lies in the field of parallel algorithms for irregular problems related to image processing, global optimization, and matrix computation.

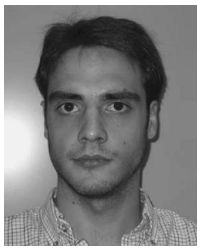

Javier Plaza received the M.S. and Ph.D. degrees in computer engineering from the University of Extremadura, Caceres, Spain, in 2002 and 2008, respectively.

He is currently an Assistant Professor with the Department of Technology of Computers and Communications, University of Extremadura, where he is a Member of the Hyperspectral Computing Laboratory. He has been a Visiting Researcher with the Remote Sensing Signal and Image Processing Laboratory, University of Maryland Baltimore County, Baltimore, and with the AVIRIS Data Facility, Jet Propulsion Laboratory, Pasadena, CA. He is the author or coauthor of more than 100 publications on remotely sensed hyperspectral imaging, including more than 20 Journal Citation Report papers, book chapters, and conference proceeding papers. His research interests include remotely sensed hyperspectral imaging, pattern recognition, signal and image processing, and efficient implementation of large-scale scientific problems on parallel and distributed computer architectures.

Gabriel Martín received the Computer Engineer degree and the M.S. degree from the University of Extremadura, Caceres, Spain, in 2008 and 2010, respectively.

He is currently a Predoctoral Research Associate with the Hyperspectral Computing Laboratory, University of Extremadura. His research interests include the development of new techniques for unmixing remotely sensed hyperspectral data sets as well as the efficient processing and interpretation of these data in different types of high-performance computing architectures.

Antonio Plaza (M'05–SM'07) received the M.S. and Ph.D. degrees in computer engineering from the University of Extremadura, Caceres, Spain.

He was a Visiting Researcher with the Remote Sensing Signal and Image Processing Laboratory, University of Maryland Baltimore County, Baltimore; the Applied Information Sciences Branch, Goddard Space Flight Center, Greenbelt, MD; and the AVIRIS Data Facility, Jet Propulsion Laboratory, Pasadena, CA. He is currently an Associate Professor with the Department of Technology of Computers and Communications, University of Extremadura, Caceres, Spain, where he is the Head of the Hyperspectral Computing Laboratory. He was the Coordinator of the Hyperspectral Imaging Network, which is a European project designed to build an interdisciplinary research community focused on hyperspectral imaging activities. He has been a Proposal Reviewer with the European Commission, the European Space Agency, and the Spanish Government. He has coedited a book on high-performance computing in remote sensing. He is the author or coauthor of around 300 publications on remotely sensed hyperspectral imaging, including more than 50 Journal Citation Report papers, 20 book chapters, and over 200 conference proceeding papers. His research interests include remotely sensed hyperspectral imaging, pattern recognition, signal and image processing, and efficient implementation of large-scale scientific problems on parallel and distributed computer architectures.

Dr. Plaza has guest edited seven special issues on remotely sensed hyperspectral imaging for different journals, including the IEEE TRANSACTIONS ON GEOSCIENCE AND REMOTE SENSING (for which he has served as an Associate Editor on hyperspectral image analysis and signal processing since 2007), the IEEE JOURNAL OF SELECTED TOPICS IN APPLIED EARTH OBSERVATIONS AND REMOTE SENSING, the *International Journal of High Performance Computing Applications*, and the *Journal of Real-Time Image Processing*. He has served as a Reviewer for more than 280 manuscripts submitted to more than 50 different journals, including more than 140 manuscripts reviewed for the IEEE TRANSACTIONS ON GEOSCIENCE AND REMOTE SENSING. He has served as a Chair for the IEEE Workshop on Hyperspectral Image and Signal Processing: Evolution in Remote Sensing in 2011. He has also been serving as a Chair for the Society of Photo-Optical Instrumentation Engineers (SPIE) Conference on Satellite Data Compression, Communications, and Processing since 2009 and for the SPIE Remote Sensing Europe Conference on High Performance Computing in Remote Sensing since 2011. He was a recipient of the recognition of Best Reviewers of the IEEE GEOSCIENCE AND REMOTE SENSING LETTERS in 2009 and the recognition of Best Reviewers of the IEEE TRANSACTIONS ON GEOSCIENCE AND REMOTE SENSING in 2010. He is currently serving as the Director of Education activities for the IEEE Geoscience and Remote Sensing Society.